

Methane adsorption and dissociation and oxygen adsorption and reaction with CO on Pd nanoparticles on MgO(100) and on Pd(111)

Steven L. Tait ^a, Zdenek Dohnálek ^b, Charles T. Campbell ^c, Bruce D. Kay ^{b,*}

^a Department of Physics, University of Washington, Box 351560, Seattle, WA 98195-1560, United States

^b Chemical Sciences Division, Fundamental Sciences Directorate, Pacific Northwest National Laboratory, Richland, WA 99352, United States

^c Department of Chemistry, University of Washington, Box 351700, Seattle, WA 98195-1700, United States

Received 12 May 2005; accepted for publication 21 June 2005

Available online 13 July 2005

Abstract

We present measurements of the desorption kinetics and dissociative sticking probability of methane on the surfaces of Pd(111) and Pd nanoparticles supported on MgO(100). A molecular beam system was used to directly probe the fraction of methane molecules that dissociate at the Pd surfaces as a function of the molecular beam energy and incident angle. Measurements on the Pd(111) surface confirm “normal energy scaling” for the methane dissociative sticking probability, consistent with an activation barrier normal to the surface, although there may be additional barriers in other degrees of freedom, but with little corrugation parallel to the surface. Sticking measurements on supported Pd particles (~3 nm wide) with the methane beam directed normal to the MgO(100) surface results in a large fraction of the methane/Pd collisions occurring on regions of the particles where the beam direction is far from the local particle surface normal, resulting in lower sticking probability. We attempt to decouple this effect from the measured sticking probabilities in order to compare the intrinsic reactivity of the Pd particles with Pd(111). We find that the sticking probability on ~3 nm Pd particle surfaces is at most twice as large as on Pd(111). This result depends on our assumption that these annealed Pd particles have the known equilibrium particle shape (truncated half octahedron). We also discuss the need for detailed structural knowledge of the particles and careful geometric analysis when probing direct collisional activation barrier crossing using molecular beams. Temperature programmed desorption studies of physisorbed (not dissociated) methane reveal that the Pd particles bind methane more strongly than Pd(111). Oxygen adsorbs on the Pd nanoparticles via a mobile, molecular O₂ precursor state which is transiently adsorbed on the MgO(100) surface. An induction period is observed on Pd nanoparticles for the titration of adsorbed O by CO gas to make CO₂ which

* Corresponding author. Tel.: +1 509 376 0028; fax: +1 509 376 6066.
E-mail address: bruce.kay@pnl.gov (B.D. Kay).

is not observed on Pd(111). This is attributed to inhibition by adsorbed O, whose saturation coverage on the Pd particles is 41% greater than on Pd(111).

© 2005 Elsevier B.V. All rights reserved.

Keywords: Methane; Oxygen; Palladium; Catalysis; Chemisorption; Sticking; Surface chemical reaction; Nanostructures

1. Introduction

Heterogeneous catalysts consisting of transition metal nanoparticles dispersed on oxide supports are pervasive in modern industrial applications, such as oil refining, organic synthesis, and reduction of greenhouse gas or other emissions. Understanding the effect that the nanometer scale confinement of matter has on catalytic properties is a current scientific challenge, since it is clear that late transition metal particles below ~ 6 nm in diameter can often have very different chemical and catalytic reactivity (normalized to metal surface area) than larger particles of the same material [1–4]. This may be due to the fact that a large fraction of the particle's surface metal atoms are in sites with coordination numbers much lower than on larger particles, or special electronic effects.

Oxide-supported Pd nanoparticles are used to catalyze low-temperature methane combustion to reduce NO_x emissions inherent to normal air combustion [5]. The reaction depends critically on the dissociation of methane molecules at the Pd surface. In a previous study of the kinetics of methane combustion over PdO_x/ZnO catalysts, it was proposed that the rate limiting step is the dissociation of the methane molecule (C–H bond activation) at a Pd site near an O atom. The observed decrease in turnover rate with decreasing particle size was attributed to a decrease in O content with decreasing PdO_x crystallite size [6]. On the other hand, catalytic reactions involving C–H bond activation in methane on similar transition metals (Ru, Rh, and Pt) show turnover frequencies that increase with decreasing particle size [7–9].

Here we study the size effects of small Pd particles for the adsorption and dissociation of methane by comparing the reactivity of Pd nanoparticles supported on MgO(100) thin films to that of a Pd(111) surface. Extensive studies of Pd particles

on MgO(100) have generated a rich supply of information about the structure of this system [2], thus making it an ideal model catalyst upon which to test Pd particle size effects in methane reactivity. Understanding nanometer-scale effects in such model catalyst systems can have a significant impact in controlled synthesis by technological catalysts.

Nanometer scale effects in Pd particles supported on MgO(100) regarding the adsorption/desorption energetics of CO molecules have been observed by Henry's research group [2,10–13]. They demonstrated that the CO oxidation reaction proceeds as on Pd single crystals for large Pd particles (13 nm), but that there is a special size effect for small particles (<7 nm), as evidenced by a higher CO_2 production rate [10]. Isothermal adsorption-desorption of CO shows similar behavior on large Pd particles (>4 nm) as on a Pd single crystal. For smaller particles (<3 nm), the desorption rate is considerably slower and it is estimated that the desorption energy is 33 kJ/mol greater [11].

Recent work on Pd deposits on $\text{Al}_2\text{O}_3/\text{NiAl}(110)$ by Freund's group has shown that CO adsorbs more strongly on small (1 nm diameter) Pd particles than on larger (3–5 nm) particles, with an adsorption energy difference of about 5–7 kJ/mol [14]. Temperature programmed desorption experiments in other groups have shown that the desorption of O_2 occurs at significantly higher temperatures on small (1–2 nm diameter) Pd and Pt particles than on larger (8–9 nm diameter) particles supported on $\alpha\text{-Al}_2\text{O}_3(0001)$ [15].

Alkane dissociation at transition metal surfaces typically proceeds via a direct collisional activation. Exceptions have been noted on (110) surfaces of Pt and Ir, where a trapping mediated dissociation pathway exists for sufficiently low incident beam energy ($<30\text{--}50$ kJ/mol, depending on surface) [16–18]. It has been argued that such a pathway cannot exist for methane dissociation

at Pt(111) due to low non-dissociative trapping [19] and also due to detailed balance theory based on measurements of associative desorption of $\text{CH}_3 + \text{H}$ at 240 K which show no indication of trapping before desorption [20,21]. The dependence of the direct dissociative sticking probability of methane on the energy and angle of incidence of the methane molecules has been addressed previously on several metal surfaces and in this paper we report this dependence for high translational energies on Pd(111) and Pd particles on MgO(100). A clear dependence of the dissociative sticking probability on the translational energy of the molecule momentum normal to the surface $E \cos^2\theta$ (i.e. normal energy scaling) has been observed for alkane dissociation at several metal surfaces including Pd(110) [22], Pt(111) [20,23–27], Ni(111) [28], Ni(100) [29], Ir(111) [30,31], Ir(110) [17,18], and W(110) [32]. Non-normal energy scaling was reported for methane and ethane dissociation at the Pt(110) surface when the molecular beam is oriented perpendicular to the $[1\bar{1}0]$ rows [16,18,33,34], where the energy scaling has been chiefly attributed to the surface corrugation. Studies of the dependence of dissociative methane adsorption on incident angle have not been done previously on Pd(111). We will demonstrate in this work that the dissociation of methane on Pd(111) exhibits normal energy scaling, as on Pt(111) [16].

The dissociative adsorption of methane on size controlled Pd particles on MgO(100) is studied here. Although Pd is commonly employed as a catalyst in methane combustion reactions, there have not been previous studies of dissociative methane adsorption on Pd/MgO model catalyst systems, nor on size-controlled Pd particles on any other support. Little is known about how metal particle size affects dissociation of small hydrocarbons, in spite of its obvious importance in a variety of catalytic processes. The reaction is studied here using molecular beams. There is a significant difficulty in the interpretation of these results due to the geometry of the particles. We will demonstrate below that on the Pd(111) surface the sticking probability of methane depends strongly on incident angle (normal energy). Thus, the particles are at a disadvantage to the flat Pd surface in a comparison of

apparent sticking probability values, since much of the particle surface is not perpendicular to the incident methane beam, which we direct normal to the MgO surface. We address this issue by using our measurements of the angular dependence on Pd(111) to compare to measurements on Pd particles. By assuming a particle shape consistent with prior observations, we then calculate what the apparent sticking probability on the particles would be if the local sticking were the same as on Pd(111), and compare this to our measurements on particles. This type of correction has not been applied previously, but should be broadly applicable to molecular beam studies of particle reactivity, so that the actual activity of the particles can be probed and compared to flat metal surfaces.

2. Experimental

2.1. Apparatus

The experimental apparatus is a molecular beam surface scattering instrument discussed in detail elsewhere [35]. This is an ultrahigh vacuum (UHV) system with base pressure of $\sim 1 \times 10^{-10}$ Torr. High quality MgO films have been produced by vapor deposition of Mg in a background of 10^{-6} Torr O_2 onto a clean and well ordered Mo(100) substrate at 600 K [36,37]. The sample is then annealed at 1000 K in this O_2 background. For film thicknesses greater than 30 layers, as employed in the present work, a sharp low-energy electron diffraction (LEED) pattern is observed and temperature-programmed desorption (TPD) experiments of CO, N_2 , and small alkane molecules demonstrate surface defect densities comparable to those obtained by UHV-cleavage of MgO crystals [35,38,39]. The low electrical and thermal conductivity of magnesium oxide makes it advantageous to use a thin film of MgO supported on Mo rather than a cleaved bulk crystal.

2.2. Pd particle preparation

Coverages of Pd here are defined in units of monolayers (ML) with one Pd ML defined as the

2 D density of Mg (or O) ions on the MgO(100) surface, 1.13×10^{15} atoms/cm², since Pd particles are known to grow in Pd(100) epitaxy on MgO(100) [40]. Pd metal (ESPI, 99.99%) was deposited onto the MgO(100) surface from an effusive cell (CreaTec) with background pressures better than 5×10^{-10} Torr. A Pd deposition rate of 0.15 monolayers per minute (ML/min) was used for the 0.15 ML Pd experiment. A deposition rate of 1.0 ML/min was used for the 0.75 and 1.4 ML Pd experiments. The deposition rate is controlled by the temperature of the effusive cell and measured directly by a quartz crystal microbalance (QCM XTM/2-Inficon). Haas et al. found the Pd cluster density to be insensitive to the Pd deposition flux for deposition on UHV- or Ar-cleaved single crystal MgO(100) samples at a comparable temperature (450 K) [41]. The MgO(100) temperature is below 40 K during Pd deposition. In this low temperature regime, the condensation coefficient of the metal is expected to be unity [3,41]. Post-deposition annealing to 600 K allows the metal adatoms to sinter and form three-dimensional islands on the surface.

For calibration of particle surface area (as described below), oxygen adsorption measurements were also made on a continuous Pd film. This was grown by deposition of ~ 100 ML Pd on Mo(100) at 40 K, then annealing to 600 K. This was a continuous Pd surface as verified by AES and will be referred to herein as “Pd film” to be distinguished from the well-defined Pd(111) surface described in the next section.

2.3. Pd(111) preparation

Experiments on the Pd(111) surface were made in a similar but separate vacuum chamber. Pt(111) was used as a substrate for growth of a thick Pd layer. After annealing to 900 K, the Pd surface was found to be of a very good quality comparable to a single crystal Pd(111) surface [42]. Surface quality was assessed by observing a sharp (1×1) LEED pattern, Kr TPD spectra with a single sharp peak, and CO TPD spectra identical to those previously published from Pd(111) single crystals [43,44]. The Pd layers were stable to 1000 K as shown by AES which showed good Pd signal,

but no Pt signal until the surface had been annealed above 1000 K. The layers were removed from the Pt surface by sputtering and annealing to >1300 K. Pd(111) surfaces of equivalent quality were repeatedly grown on the same substrate.

2.4. Molecular adsorption and temperature-programmed desorption experiments

TPD measurements were made by depositing CO₂, CO, or CH₄ on MgO(100), Pd(111), or on Pd particles on MgO at low temperature (30 K). The molecule of interest was deposited on the sample using a room temperature, unseeded molecular beam, which was quadruply pumped and impinged on the surface at normal incidence. The sample was then heated at a controlled rate (0.6 K/s) and quadrupole mass spectrometers (QMS) were used to measure the desorption rate of the molecules from the surface.

Adsorption of CO, CO₂, or CH₄ on the MgO(100) surface in each case gave rise to a very distinct monolayer (ML) peak in TPD which saturated first and was cleanly separated from any higher-coverage TPD peaks [35,38,39]. These saturation ML peaks were time-integrated to find the QMS signal corresponding to 1 ML of each molecule. In this way, time-integrated QMS signals were calibrated to units of ML CO, ML CO₂ or ML CH₄ for use in calculation of coverages and sticking probabilities as discussed below. All CO and CO₂ TPD measurements were made using a QMS that is enclosed in a shroud which has an entrance orifice in a line-of-sight with the sample. As molecules from the sample enter this orifice to the QMS, they make several collisions with the shroud surfaces before being deflected into the QMS ion source. In this way, the molecules are thermalized to the shroud temperature (constant in all experiments, ~ 350 K) before being detected, so that no correction to the QMS signal is necessary to account for differences in their initial velocities or temperature. CH₄ TPD measurements were conducted in the same way for TPD measurements related to the adsorption of methane on the various surfaces studied. Control CH₄ TPD measurements were also made with the QMS positioned in the same non-line-of-sight position used to measure

the CH₄ beam flux in the CH₄ dissociation measurements described below, in order to calibrate the time-integrated signal at that QMS position into units of ML CH₄.

Previous experiments using neutron diffraction methods have found that the monolayer of methane adsorbs on MgO(100) in a $\sqrt{2} \times \sqrt{2}R45^\circ$ square layer [45,46]. This layer has a density of $5.64 \times 10^{14} \text{ cm}^{-2}$, which we use to convert the methane exposure from units of ML to the number of C atoms per cm². The ML packing densities for CO and CO₂ on MgO(100) were found by multiplying the CH₄ density by the ratio of the liquid methane molar volume (37.94 cm³/mol) to the liquid CO or CO₂ molar volume (35.42 cm³/mol or 61.13 cm³/mol, resp.) raised to the 2/3 power [47]. In this way, ML densities of $5.92 \times 10^{14} \text{ CO/cm}^2$ and $4.11 \times 10^{14} \text{ CO}_2/\text{cm}^2$ were obtained. In all three cases, the number of molecules per cm² equals the corresponding number of C atoms per cm², so these units are completely interconvertible when doing C atom balances below.

2.5. Methane dissociation experiments

Measurements of methane dissociation on the Pd(111) surface and on MgO-supported Pd particles were made using supersonic molecular beams of methane in separate but similar vacuum systems. For sticking probability measurements on Pd(111), the incident angle of the methane beam was varied from 0–56° from sample normal, but all measurements on the Pd particles were made with the beam at normal incidence to the MgO(100) surface. Beam energies from 38 to 71 kJ/mol were obtained by varying the temperature of the beam nozzle from 470 to 885 K with a fixed seeding in 99% He. Since the beam was mostly composed of He, the translational energy was determined by the formula for a beam of atoms (ideal gas) given by

$$E = \frac{5}{2}RT_{\text{nozzle}} \left(\frac{M}{xM + (1-x)m} \right), \quad (1)$$

where T_{nozzle} is the beam nozzle temperature, M is the mass of the seed molecule (methane), m is the mass of the carrier gas (He), and x is the seeding ratio (0.01 in this case) [48,49]. Under our nozzle

expansion conditions, the rotational temperature of the methane is expected to be <30 K and the vibrational temperature nearly equal to the nozzle temperature.

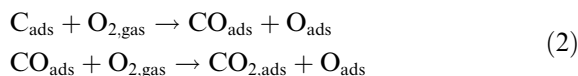
The amount of CH₄ dosed to the surface was controlled by beam shutters and determined by measuring the methane signal with a background (i.e., not line-of-sight to sample) mass spectrometer. The average QMS signal during the methane dose for $T_s > 500 \text{ K}$ is thus proportional to the average methane beam flux, since the sticking probability is small. Methane TPD experiments after methane adsorption (non-dissociative physisorption) at 30 K were made in this same sample and QMS geometry. The resulting TPD peak area for the saturated methane ML (see above) was used to calibrate the beam flux into units of ML methane per second. From this, methane exposures were determined simply from the time length of the methane dose, in units of ML CH₄ or C atoms per cm².

The activity of the Pd surfaces for dissociation of methane was explored by measuring the fraction of incident molecules that dissociatively adsorb on the surface from a given methane exposure. The amount of dissociated methane was quantified by measuring the resulting coverage of surface C (C_{ads}) by titrating with an O₂ beam (to make CO and CO₂) as described below. The Pd(111) sample was held at 550 K during methane beam exposures. Elevated sample temperatures were used to prevent accumulation of H and CO, based on the known TPD temperatures for H and CO on Pd surfaces [11,43,50,51]. A slightly lower temperature (500 K) was used for the Pd particles to minimize particle sintering during the experiments, as discussed below. Luntz and Harris compiled molecular beam experiments of CH₄ dissociation on Pt(111) vs. sample temperature and beam energy [52], which allows us to argue that this small difference in temperature has less than a 20% effect of the observed rates, as follows. The absolute sticking measurements in that work are very similar to our measurements on Pd(111) at the same sample temperature and beam energy conditions. In their results for CH₄ normal incident energy of 60 kJ/mol, the initial sticking probability decreases by less than 20% when the

sample temperature was decreased from 550 to 500 K. However, the relative change in initial sticking with sample temperature has a strong dependence on normal incident energy of CH₄: at 41 kJ/mol the effect was twice as large and at 123 kJ/mol the effect was much smaller (3% change) [23,25,52]. Thus, we expect that the difference in sample temperature will have a small effect on CH₄ sticking probability measurements at the highest beam energy (71 kJ/mol) in our study, but may be a larger effect at smaller energies. If the Pd(111) experiments had been done at 500 K rather than 550 K, we would expect that the sticking results would be smaller by less than 20%.

2.6. Quantifying C_{ads} coverage by titration with O₂

The amount of adsorbed C produced on the Pd surfaces by each methane exposure was determined by titrating it from the surface using an O₂ beam, with the surface temperature maintained at 550 K (or 500 K in the case of the Pd particles). The oxygen molecules dissociate at the Pd surfaces and react with the C_{ads} to form the products CO and CO₂:



By C_{ads} above, we do not necessarily imply that this surface C is in the form of isolated, H-free C adatoms. The resulting transient desorption signals of CO (m/e = 28) and CO₂ (m/e = 44) products from the surface were measured by line-of-sight QMS. Fig. 1 shows the CO₂ desorption signal measured on the 0.15 ML Pd particles for two methane exposures. Also shown in Fig. 1 is a measurement of the background signal, done by moving the sample out of the molecular beam path during the methane exposure, but putting it back into the beam for the C_{ads} titration step. In that case we see that the CO₂ background signal is approximately a square wave corresponding to the time of the O₂ exposure (indicated in Fig. 1). The CO signal (not shown here) followed a similar behavior. During each experiment, the oxygen beam was left on until the CO₂ and CO signals

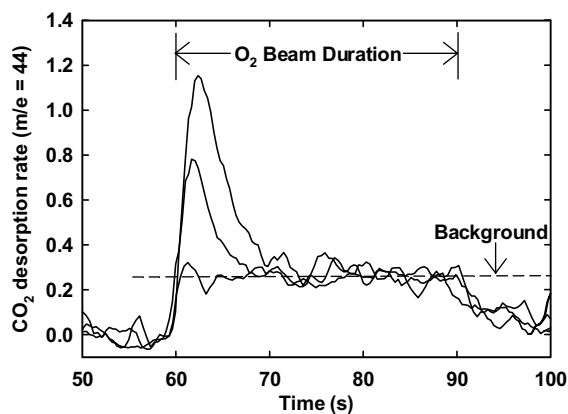


Fig. 1. C_{ads} titration by O₂ molecular beam [Reaction (2)]. Transient CO₂ desorption signal measured by line of sight QMS and plotted vs. time. The O₂ beam shutter was opened at 60 s and closed at 90 s in these experiments as indicated in the figure. A different methane exposure was used for the two experiments with larger CO₂ desorption rates. In the case of the third experiment, the sample was moved out of the beam path during the methane exposure and put back in position for this C_{ads} titration step in order to obtain a background CO₂ measurement. The dashed line in the figure indicates the approximate background level subtracted from each experiment before integrating to obtain the C_{ads} coverage.

return to these baseline levels (indicated by dashed line in Fig. 1), indicating that the C_{ads} had been completely titrated to CO and CO₂. The area under these desorption signals was integrated after subtracting from the signal this constant baseline value, measured by the average signal intensity near the end of the O₂ exposure for each experiment (indicated approximately by dashed line in Fig. 1).

The observed transient CO and CO₂ production signals were normalized to units of ML CO and ML CO₂ using the TPD ML calibration discussed above. This assumes the same angular distribution of desorption in the molecular CO and CO₂ TPD experiments as in the C titration experiment. The QMS was positioned at about 30° from sample normal, near the so-called magic angle (~35°) [53], to minimize the effect of any possible differences in angular distribution, e.g. due to differences in desorption temperature (550 K in C titration experiments vs. 55 K in CO or 100 K in CO₂ TPD experiments). The m/e = 28 signal was corrected to subtract the amount of m/e = 28

due to cracking expected from CO₂ [(m/e = 28 signal due to CO₂) = (11% of m/e = 44 signal)]. These CO₂ and corrected CO transient signals, thus normalized to their ML signals, were converted to C atoms per cm² as described above, giving directly the number of methane molecules per cm² dissociated by each beam exposure.

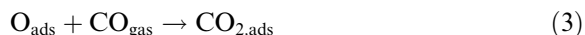
As the amount of deposited C_{ads} increased, more CO and CO₂ were observed. However, the sticking probability measurements that we report here were all made in the limit of small CH₄ exposures (i.e. initial sticking probability). In this limit, the CO/CO₂ production ratio was always observed to be about 0.45 for the 0.75 and 1.4 ML Pd coverages on MgO(100). For experiments with only 0.15 ML Pd, the CO₂ and CO signals were weak. In order to maximize our signal to noise ratio for this Pd dose, the QMS was set to record only m/e = 44 (CO₂), and we assumed that CO was produced in this same CO/CO₂ ratio.

2.7. O₂ saturation on Pd and O_{ads} titration by CO

In order to estimate the total Pd surface area of the Pd particles, we determined the saturation coverage of O_{ads} on the Pd/MgO samples as follows. Following the methane exposure in an initial sticking probability measurement such as described above, the surface had a low C_{ads} coverage. This C coverage was titrated with an O₂ beam as described above, and the O₂ beam was left hitting the surface for long enough to saturate the now carbon-free Pd surfaces with oxygen. For the O₂ beam flux used here, the CO and CO₂ QMS signals decreased back to background by <15 s exposure, and the O₂ exposure was allowed to continue for another 15 s (see Fig. 1). This is a total exposure of about three times that required to saturate the C-free Pd with oxygen, which on the Pd(111) surface corresponds to ~0.25 ML of O_{ads} and is achieved after <1 Langmuir exposure [54,55]. The O₂ QMS signal due to the non-sticking O₂ beam showed an initial King and Wells-type uptake period when the beam was started [56] which clearly saturated in <20 s, further confirming that 30 s was sufficient to saturate the surface with oxygen.

This adsorbed oxygen was then removed from the surface by exposure to a CO beam, producing

an easily measured CO₂ transient according to the reaction:



This desorption of CO₂ was measured by the QMS, and its integrated area, when compared to the molecular CO₂ desorption peak area in TPD, provides the number of O_{ads} atoms per unit MgO area. Since oxygen does not adsorb on MgO(100) but does adsorb on the Pd particles, this quantity will be used to estimate the total surface area of the Pd particles per unit MgO area (excluding the interfacial area between the particle and the MgO substrate), as described below.

3. Results and discussion

3.1. Growth of particles

Fig. 2 shows the fraction of the MgO(100) surface area that is covered by Pd particles (i.e., the “Pd area fraction,” f_{Pd}), as a function of Pd coverage. These area fractions were estimated from the measured saturation oxygen coverage, assuming (1) that the saturation oxygen coverage is proportional to the exposed Pd surface area, and (2) that the particles have their equilibrium shape as determined by Henry et al. [2,3], which is a truncated half octahedron with size-independent aspect ratio of 0.4. (This assumption is justified below.) For this shape, the ratio of its exposed surface area (i.e., accessible for oxygen adsorption) to its footprint area (i.e., the projection of its area onto the MgO surface) is 1.6. Dividing the total Pd surface area per unit MgO area by this factor yields f_{Pd} . The total Pd surface area per unit MgO area was determined by dividing the saturation oxygen coverage by that for a continuous Pd film (formed by deposition of ~100 ML Pd and annealing to 600 K), for which this area ratio is taken to be one.

In Section 3.2 below we show that the saturation coverage of oxygen per unit Pd area was 41% larger on the nanoparticles studied here compared to the continuous Pd film. An adjustment to account for this difference in saturation oxygen coverage was made to obtain the Pd area fractions shown in Fig. 2. The solid curves in Fig. 2 are

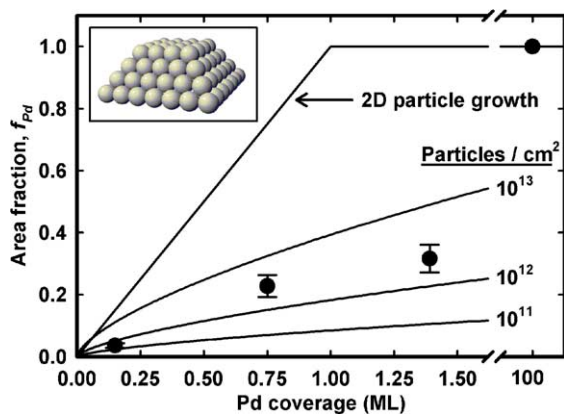


Fig. 2. Pd area fraction vs. Pd coverage. Area fraction was calculated from O_{ads} titration experiment [see Reaction (3)] and was defined to be unity for 100 ML Pd film. Points for particles have been corrected for difference in O saturation coverage relative to Pd film, as discussed in the text. Error bars correspond to one standard deviation in the set of O_{ads} titration experiments. Lines represent calculations of area fraction vs. coverage for particles of equilibrium shape at the number density indicated. Inset: Ball model of Pd nanoparticles in truncated square pyramid configuration with aspect ratio of height/base width = 0.4, as proposed by Henry et al. [2] Top surface of particle is truncated by the (100) plane and sides are (111) planes. There are 126 atoms in this particle and it has a base width of 1.79 nm and a height of 0.78 nm.

calculations of the area fraction versus Pd coverage assuming the same equilibrium particle shape for the particle number densities shown.

The Pd particle number density and average size were estimated from f_{Pd} , using the total volume of deposited Pd per unit MgO area measured by the QCM. For the Pd coverages studied (0.15, 0.75, and 1.4 ML), the particle widths (at their base) were found to be 3.2 ± 0.7 , 2.6 ± 0.4 , and 3.4 ± 0.5 nm, respectively, with number densities of $3.5 \mp 2.2 \times 10^{11}$, $3.4 \mp 1.6 \times 10^{12}$, and $2.7 \mp 1.1 \times 10^{12}$ particles/cm², respectively. The stated errors correspond to the uncertainty in the area fraction (one standard deviation of the measurement set), represented by the error bars in Fig. 2, and are not intended to indicate the width of the particle size distribution, which we have taken to be zero (uniform particles) in this calculation. These results indicate a low number density of particles for the smallest coverage (0.15 ML). As the Pd coverage increased to 0.75 ML the number den-

sity of particles increased. Upon further increase of the coverage to 1.4 ML no significant change in number density was observed, indicating that we had reached the saturation particle density on this surface. These island densities are consistent with the range of earlier microscopy observations for Pd nanoparticles on similarly prepared MgO surfaces [2,3,41]. The size of the particles does not change between 0.15 and 0.75 ML of Pd within the error bar of our results. However, upon increasing the coverage from 0.75 to 1.4 ML the particle size increased as the number density stayed nearly constant. The accuracy of this method for determining absolute particle sizes is probably only $\pm 30\%$. Generally, an increase in size with coverage is expected for fixed growth conditions [2].

Auger electron spectroscopy (AES) and X-ray photoelectron spectroscopy (XPS) were used to gauge the degree of particle dispersion by comparing the Pd/Mg peak amplitude ratios for 0.15 ML to 1.4 ML of Pd. In each case, the sample was cooled below 40 K (after annealing to 600 K) to make AES or XPS measurements. The Pd/Mg AES and XPS ratios increased by factors of 11 and 15 respectively between 0.15 and 1.4 ML Pd. Using well-established formulae for the signal intensity expected for a given electron energy and adsorbate film [57], together with published values for electron inelastic mean free paths [58], we calculated these Pd/Mg ratios assuming different particle sizes (with their corresponding number density set by the total Pd coverage) and again assuming the equilibrium particle shape. The results showed that these large increases in the Pd/Mg ratios with Pd coverage could only be reproduced if the particle size stays nearly constant but their number density increases ~ 10 fold with Pd coverage. This agrees well with number densities obtained from the O titration experiments (discussed above). The absolute values for these number densities (and particle sizes) could not be extracted from fitting these ratios with as much accuracy as using the saturation oxygen coverages, due to the uncertainty in the ratios of the elemental sensitivity factors.

Images have been obtained previously with transmission electron microscopy for Pd/MgO(100) by

Henry et al. [2,3] The observed equilibrium shape of the Pd particles on MgO(100) has been shown to be a truncated half octahedron with constant height/base ratio (0.4) in the particle size range 1–10 nm [2,3], which is consistent with the Wulff-Kaichew construction [59]. The half octahedron is truncated by the (100) facet on the top (and bottom) of the Pd particles, and their sides are (111) facets. A ball model of a particle with this shape and a base width of 1.8 nm is shown in the inset of Fig. 2. It has been observed by He scattering measurements that the onset of surface diffusion for the formation of Pd clusters on MgO(100) occurs below 400 K (faceting of particles observed) [60]. It has also been noted that large Pd clusters (~ 8 ML deposit) deposited at low temperature and annealed up to 673 K (total anneal time 2 h) are able to form well defined crystalline facets, but are not able to reach the equilibrium particle shape [3]. The time required for a crystallite to reach its equilibrium shape has been shown to be proportional to the radius of the crystal to the fourth power and also proportional to temperature ($\tau \sim r^4 T$) [59]. Since our Pd particles are small ($r < 3$ nm), those results indicate that our annealing treatment (30 s at 600 K and then minutes to hours at 500 K) should be sufficient to reach the equilibrium shape. Henry et al. [40] estimated the relaxation time for small nanoparticles ($r = 5$ nm) deposited at 673 K to be about 3 s. They further note that flat particles (formed by deposition at low T) have a much smaller diffusion coefficient and so relaxation times will be 100 times longer. Using their estimate of the diffusion coefficient for flat particles and accounting for the difference in anneal temperature and especially for the difference in particle size, we estimate that the relaxation time for our particles is only ~ 30 s, which is on the order of the annealing time we used at 600 K. Furthermore, since the relaxation time is proportional to temperature [59] the several minutes to hours at 500 K will allow ample time to reach the equilibrium particle shape.

In some cases the same Pd/MgO surface was used for several consecutive methane dissociation measurements, in each case restarting from the clean surface generated by O_2 titration of the C_{ads} and subsequent CO titration of the O_{ads} , all at

500 K. We observed that the saturation oxygen coverage (exposed Pd surface area) decreased slowly as a function of the amount of time the Pd/MgO sample was held at 500 K. This indicates that the surface area of the particles decreased slowly due to sintering. Most methane dissociation experiments were conducted within 5 h of the Pd dose, where the saturation oxygen coverage decreased by $< 10\%$. This near constancy verifies the fact that nearly the same Pd/MgO surface could be regenerated in this way. Nevertheless, to correct for the slight decrease in the Pd area fraction with time, the value used with each methane sticking measurement was the one determined from the subsequent O_{ads} saturation coverage measurement for that run, not from the average f_{Pd} in Fig. 2.

To summarize, these growth studies indicate that for the Pd coverages studied here, the particles are near their equilibrium shape, with a width of ~ 3 nm that probably increases weakly with coverage and a number density that increases strongly with coverage until reaching saturation around $\sim 3 \times 10^{12} \text{ cm}^{-2}$.

3.2. Kinetics of oxygen adsorption and O_{ads} titration by CO

The kinetics of the adsorption of oxygen on the Pd particles and continuous Pd film at 500 K were monitored using the King and Wells method [56], by measuring the non-sticking fraction of an O_2 molecular beam striking the initially clean Pd/MgO(100) surface. The resulting sticking probabilities versus coverage are shown in Fig. 3. Coverage was determined by integrating the sticking probability and normalizing to 0.25 ML for the Pd film. The same normalization constant was used for the Pd particle data, then these data were further normalized by the measured area fraction and the ratio of surface area to footprint area of the particles (1.6) so that this coverage represents the density of O atoms per surface Pd atom. As can be seen, the sticking probability is initially high (~ 0.7), and decreases rapidly with coverage. The results on the continuous Pd film (pre-annealed to 600 K) are similar to those reported previously for Pd(111), except that there S_0 was only

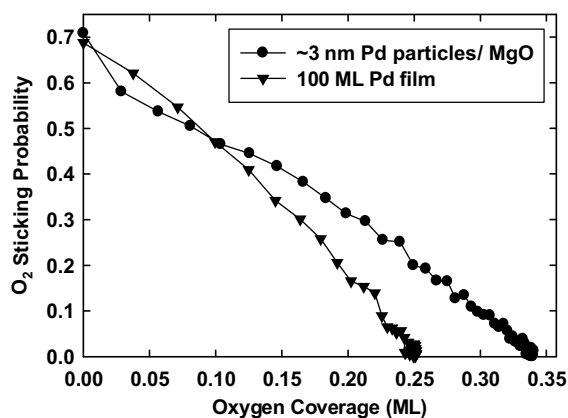


Fig. 3. Oxygen sticking probability vs. oxygen coverage on Pd nanoparticles/MgO (circles) and on a continuous Pd film (triangles). The coverage was determined by integrating sticking probability vs. time and normalizing to 0.25 ML in the case of the film. The oxygen coverage on the particles was normalized by the same factor as well as the area fraction (0.35) and ratio of total Pd surface area to footprint area (1.6) to yield the O on the Pd particle surfaces. That coverage is 0.34 ML, consistent with the saturation coverage from the O_{ads} titration kinetics (see Section 3.2).

~ 0.4 for $T_S = 500$ K [54]. Interestingly, the initial sticking probabilities on the surfaces containing Pd particles (~ 0.7) exceed the fractional area of the MgO that is covered by Pd particles (0.35). Since O_2 does not irreversibly adsorb on MgO(100) at this temperature, this proves that O_2 molecules must transiently adsorb on the MgO(100) surface and migrate to the Pd particles, where they irreversibly stick. The same reverse-spillover effect has been reported previously for CO adsorption on Pd/MgO(100) [11].

Fig. 4 shows representative data from the O_{ads} titration experiments used to measure the saturation oxygen coverage (as described in Section 3.1) for each of the three Pd coverages: 0.15, 0.75, and 1.4 ML, as well as for the 100 ML Pd film. Here, the Pd surfaces were first saturated with O_{ads} using an O_2 beam, and then exposed to a CO beam, while monitoring the CO_2 signal. Also shown is a QMS signal measured for a CO_2 beam reflected from the Pd film at high temperature (i.e. with negligible sticking), which serves as a measure of the instrument response time to a step increase in CO_2 flux from the sample. We see that in the O titration from the 100 ML Pd film, the QMS

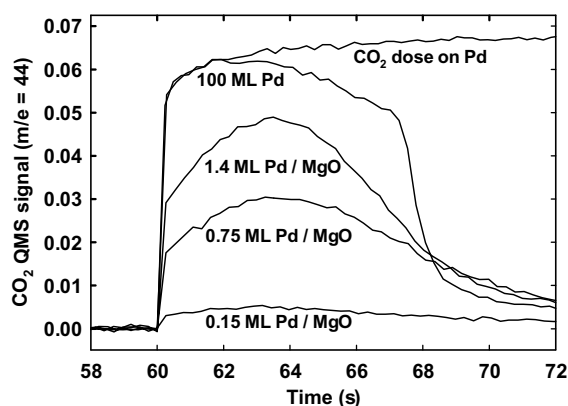


Fig. 4. CO_2 QMS signal vs. time during the titration of O_{ads} at $T_S = 500$ K by a CO beam on Pd nanoparticles prepared by deposition of 0.15, 0.75, and 1.4 ML Pd as well as on a 100 ML Pd film. At $t = 60$ s, a CO molecular beam of steady flux was impinging on the sample to react with adsorbed oxygen. A CO_2 dose on a continuous Pd film held at a temperature well above the CO_2 desorption temperature is also shown to illustrate the time response of the QMS instrument to the reflected CO_2 beam. This curve has been arbitrarily normalized to line up with the 100 ML Pd curve. We see that in the case of the Pd film, the CO_2 signal rises to its maximum as fast as the instrument response to a step-function CO_2 beam. The kinetics of the reaction are clearly quite different on the nanoparticles, where the signal initially rises only to about 60% of its maximum value, then rises more slowly to the maximum after about 3–4 s. We attribute this difference to a larger saturation coverage of O_{ads} on the nanoparticles compared to the flat Pd surface, which inhibits CO adsorption and reaction.

CO_2 signal rises as quickly as this instrument response function. This transient kinetic response kinetics is identical to that reported for CO titration of a saturated oxygen adlayer on Pd(111) at 500 K [61], where it is known that saturation oxygen is in a $p(2 \times 2)$ structure with $\theta_O = 0.25$ ML [54,55]. In contrast, for the particles the CO_2 signal rises immediately to only $\sim 60\%$ of the maximum value, then maximizes on a much slower time scale. This striking difference in the kinetics of the CO oxidation [Reaction (3)], whereby for nanoparticles there is an induction period before maximum reaction rate is reached, will be interpreted here as indicating that there is a larger O saturation density on the Pd particles compared to Pd(111) and the continuous Pd film. This is consistent with prior, more direct measurements, in which the saturation coverage of oxygen on

small alumina-supported (<2 nm) Pd particles was more than 60% larger than on large, bulk-like particles (>9 nm), where the authors attributed this difference as possibly being due to higher oxygen coverages on the less-closely packed Pd (100) and (110) surfaces [15]. Thus, we attribute the induction period on the nanoparticles in Fig. 4 to a higher oxygen coverage (above 0.25) which inhibits CO adsorption and thus the initial titration rate. (CO adsorption is required for this reaction but is not inhibited by $\theta_{\text{O}} = 0.25$ [61].) We further assume that the maximum rate is only reached when the coverage falls to ~ 0.25 .

By integrating the area under the curves in Fig. 4 on either side of their maxima, we estimated the initial saturation coverages of oxygen relative to that coverage where the rate maximizes (~ 0.25). This showed that the saturation coverage of O_{ads} on the nanoparticles was $41 \pm 10\%$ larger than on the continuous Pd film or Pd(111). Accounting for this increase leads to a decrease in the calculated Pd area fraction f_{Pd} for the Pd particles relative to the continuous Pd film (Fig. 2).

3.3. Methane molecular adsorption on Pd nanoparticles and on Pd(111)

Fig. 5 shows TPD spectra of molecular methane desorption after adsorption of >2 ML methane to the following surfaces at 33 K: (a) the clean MgO(100) surface, (b) Pd particles formed by deposition of 1.4 ML Pd at 40 K, (c) surface (b) after annealing to 600 K, and (d) the Pd(111) surface. The sharp multilayer desorption peak at 38 K is excluded here. These curves have been offset along the y -axis for clarity. A thin dashed line for each curve indicates its zero signal level. The desorption feature at 48 K corresponds to methane desorption from MgO(100) terraces, and the shoulder at 60 K in curve (a) is due to defects on the clean MgO surface [35,39]. As Pd coverage increases, this MgO peak decreases and other features at 55–85 K appear which we attribute to desorption from Pd surfaces. The peak at 66 K for Pd(111) agrees with prior reports [62]. After annealing the Pd particles, the 48 K TPD peak for MgO(100) increased in size [curves (c) vs. (b)], indicating that the particles have sintered,

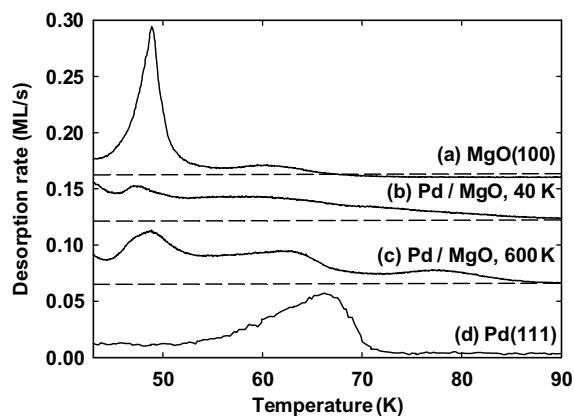


Fig. 5. Temperature programmed desorption (TPD) spectra of methane after a multilayer methane dose below 40 K to: (a) MgO(100), (b) 1.4 ML Pd deposited on MgO(100) at 40 K, (c) 1.4 ML Pd/MgO(100) annealed to 600 K, and (d) a Pd(111) thin film.

exposing more of the MgO surface area, as expected [50,63].

There are two desorption peaks from the Pd particle surfaces. Annealing sharpens these peaks, which we attribute to surface ordering. The larger peak is at a lower temperature than for Pd(111), indicating that methane binds more strongly to Pd(111) than to majority sites on nanometer-scale particles. We interpret this as being due to the higher polarizability of bulk Pd than nanoparticles, since the non-dissociative methane–Pd attraction (physisorption) is probably due to instantaneous dipole-induced dipole interactions. The TPD peak at ~ 78 K on the Pd particles corresponds to $\sim 20\%$ of the intensity from Pd sites in curve (c), due to minority sites on the Pd particles which bind methane more strongly than Pd(111) and may include Pd(100) sites. In these low-temperature TPD experiments with a thermal methane beam, no dissociation of the methane was observed. The methane desorption signal for Pd(111) does not fall all the way to zero between the multilayer and monolayer peaks. This is due to compression of the first layer of methane molecules as the second layer of molecules forms [64].

In principle, one could use the intensities of the methane TPD peaks from Pd sites, relative to that from the MgO terraces, to determine f_{Pd} . However, in this case it is impossible to unambiguously

distinguish the TPD signal intensity of methane desorption from Pd and from MgO surfaces. This is probably due, in part, to TPD intensity in the 55–85 K range due to methane bound to both Pd and MgO at particle edges. These would lead to overcounting the Pd surface area and yield erroneously high values for f_{Pd} .

3.4. Methane sticking on Pd(111)

Sticking on Pd(111) was measured for three beam energies and at four angles of incidence. Fig. 6(a) shows a log plot of the measured initial dissociative sticking probability as a function of beam energy at a sample temperature of 550 K. The different symbol styles correspond to different angles of incidence. The sticking probability here is calculated by dividing the number of C atoms per unit area removed from the surface by the O_2 beam (C_{ads} titration) by the number of methane molecules which collided with the surface per unit area (CH_4 dose). We have drawn a linear regression to these data points to emphasize that there is not a clear scaling relationship between total beam energy and sticking probability.

Fig. 6(b) plots the initial dissociative sticking probability, S_0 , as a function of “normal beam energy,” defined to be $E_{\text{normal}} = E \cdot \cos^2\theta$, which can be interpreted as the fraction of the beam kinetic

energy corresponding to the component of its momentum normal to the surface. Here again we draw a linear regression (solid line) through the data points and see a much better correspondence, indicating normal energy scaling in this case. This fit function is

$$\log_{10} S_0 = -5.17 + 0.0492 \left(\frac{E_{\text{normal}}}{\text{kJ/mol}} \right). \quad (4)$$

However, we note that the sticking probabilities at the two highest angles of incidence seem to follow a different trend than the measurements made at the two lower angles of incidence. If we exclude the high angle points from the linear regression (dashed line), we see a much better fit to the data points:

$$\log_{10} S_0 = -5.97 + 0.0619 \left(\frac{E_{\text{normal}}}{\text{kJ/mol}} \right), \text{ or} \quad (5a)$$

$$S_0 = 1.07 \times 10^{-6} e^{0.143 \left(\frac{E_{\text{normal}}}{\text{kJ/mol}} \right)}. \quad (5b)$$

We will use this trend line in the analysis discussed below. The reason that these high angle points have sticking probability values higher than this trend line could be due to a small number of defect sites on the surface. The sticking observed at these defect sites (e.g. step sites) might have less angular dependence than sticking on the flat Pd terraces. If a defect density of 1% is sampled with the beam at 56° and sticking at defects is the same

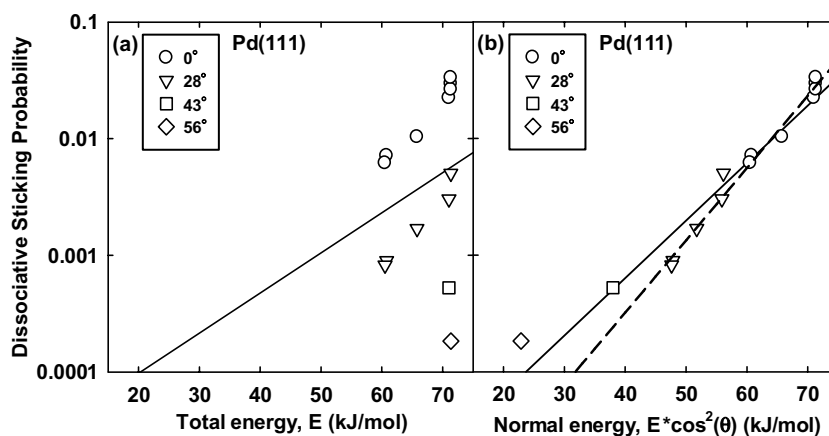


Fig. 6. Initial methane dissociative sticking probability, S_0 , on Pd(111) at $T_s = 550$ K. Symbols correspond to different incident angles θ of the methane beam as indicated in the legend. (a) S_0 vs. methane beam energy. Solid line is linear regression to data points. (b) S_0 vs. “normal energy,” defined as $E \cdot \cos^2\theta$. Solid line is linear regression to all data points [Eq. (4)]. Dashed line is a linear regression which excludes points at 43° and 56° incident angle [Eq. (5)].

as on terraces at normal incidence (0.02–0.03) (i.e., sticking at step defects may be insensitive or less sensitive to incident angle), then the net sticking probability would be 0.0002–0.0003 (entirely from defects), which is about what we observe at 56°. This sticking probability value is also the difference between the observed sticking probability at 43° and the linear fit line (dashed line) through the low angle points.

The dissociative sticking probability on Pd(111) is 0.0279 for a beam energy of 71 kJ/mol at normal incidence. Sticking probabilities have previously been reported for methane dissociative adsorption on Pd(110) by Valden and coworkers [22,65] under similar experimental conditions ($T_{\text{sample}} = 500$ K, $T_{\text{nozzle}} = 700$ K). They found it to be ~ 0.03 for normal beam energies of about 70 kJ/mol [22,65], consistent with the present results. Dissociative sticking of methane on Pt(111) has been measured to be 0.02–0.06 at 70 kJ/mol (normal) beam energy [26,27], also in agreement with our measurement.

Sticking probabilities were also measured on a Pd film formed by deposition of 100 ML Pd on Mo(100) at 40 K, followed by annealing to 600 K. Sticking probability at normal incidence at 71 kJ/mol was 0.0363, 30% higher than the measured value on Pd(111). However, it had a much weaker dependence on incident angle than for normal energy scaling, suggesting that this cannot be simply interpreted as reflecting the behavior of a Pd(100) surface (i.e. this film may have a high defect density and/or roughness which weakens the incident angle dependence of the sticking probability).

The strong dependence of the sticking probability on local angle of incidence, as observed on Pd(111), will have a significant effect on the measurement of sticking on Pd particles. In the case of the particles a significant fraction of the methane beam strikes the Pd nanoparticle surfaces at angles far from normal incidence.

3.5. CH_4 dissociation on Pd nanoparticles on MgO(100)

In order to correctly calculate the dissociative sticking probability of methane on the Pd parti-

cles, we need to determine the fraction of the methane beam which is incident on Pd surfaces. As shown below, the dissociation of the methane is a strong function of incident kinetic energy and so the methane that impinges on the bare MgO surface between Pd particles is not expected to dissociate (i.e. we assume here that there is no oxide-precursor mediated dissociation of CH_4). Control experiments on Pd-free MgO(100) proved that the rate of dissociative sticking of methane on MgO(100) was negligible.

The Pd area fraction f_{Pd} , derived above, provides the fraction of the MgO substrate covered by Pd particles and is therefore equivalent to the probability that a methane molecule incident on the sample surface will strike a Pd particle. In this way, we determine how much methane is incident on the Pd surfaces and exclude from the sticking calculation that fraction of the methane beam which impinges on the bare MgO substrate surface. Then the initial sticking probability can be calculated as

$$S_0 = \frac{N_{\text{C,adsorbed}}}{f_{\text{Pd}} \cdot N_{\text{C,exposed}}}, \quad (6)$$

where $N_{\text{C,adsorbed}}$ is the number of C atoms per cm^2 of sample area as determined by the C_{ads} titration experiment described in Section 2.6 and $N_{\text{C,exposed}}$ is the number of C atoms exposed (i.e., CH_4 molecules dosed) per cm^2 of sample area. Hence, the sticking probability values presented here can be interpreted to represent the probability that a methane molecule, incident on the Pd surface at a given beam energy and incident angle, will break a C–H bond and dissociatively adsorb on the surface. In the case of the Pd(111) surface, no area fraction correction was necessary in calculating the initial sticking probability from the experimental results [i.e., $f_{\text{Pd}} = 1$ in Eq. (6)].

Sticking probability measurements on the Pd particles were made at incidence normal to the MgO(100) substrate for various beam energies. These are plotted on a log scale in Fig. 7. Here the different plot symbols correspond to different Pd coverages. For the 0.15 and 1.4 ML Pd particles, sticking probability measurements were made at a wide range of beam energies. The results for the two Pd coverages are statistically indistinguish-

able, consistent with their particle sizes being nearly the same but at different densities, as discussed above. For the 0.75 ML Pd particles, measurements were only made at 71 kJ/mol, but are in good agreement with the other Pd coverages. The sticking probability increases exponentially with beam energy due to the activation barrier for C–H bond fission. The points at 71 kJ/mol are averages of many experiments. Other points represent a single measurement. We have fit all of these points to the line

$$\log_{10} S_0 = -(6.40 \pm 0.18) + (0.0620 \pm 0.0027) \left(\frac{E_{\text{normal}}}{\text{kJ/mol}} \right). \quad (7)$$

For comparison, the linear regression to the sticking probability points for Pd(111) [dashed line in Fig. 6(b)] is reproduced here as a dashed line. We see that the sticking probabilities on

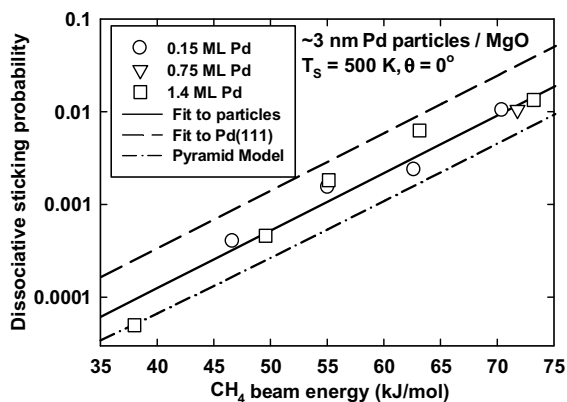


Fig. 7. Initial methane dissociative sticking probability on Pd nanoparticles at $T_s = 500$ K as a function of methane beam energy which was incident normal to the MgO(100) substrate. Nanoparticle results from three Pd coverages are shown: 0.15 (circles), 0.75 (triangles) and 1.4 (squares) ML. Measurements on 0.75 ML Pd were only made at 71 kJ/mol. Points at 71 kJ/mol are averages of several experiments, other points represent single experiments. Solid line is a linear regression to the points [Eq. (7)]. After calculating this regression, the points at 71 kJ/mol were offset along that slope for clarity. Dashed line is the linear regression to the sticking probability on the Pd(111) surface [Fig. 6(b), dashed line]. This function was used to calculate apparent sticking on nanoparticles of the equilibrium particle shape discussed in the text assuming that the sticking on the particle surfaces is the same as on Pd(111) (dash-dot line).

Pd(111) are higher by a factor of ~ 3 than those on the particles for any beam energy. However, it is important to remember that the particles sample methane molecules with much lower energy (in the direction of the local surface normal) in this measurement due to the high angle of incidence of the methane beam over much of the particle surface. The incident angle of the methane beam on the sides of the particles will be greater than on the tops of the particles or on the continuous Pd(111) surface. A larger incident angle of the methane beam (relative to the local particle surface normal) in a given region of a particle will have two implications. First, the beam flux will be locally smaller in that region of the particle surface than the average flux to the surface. Second, the sticking probability itself will decrease with incident beam angle. As discussed in Section 3.4 above, normal energy scaling was observed in measurements of S_0 as a function of incident angle on Pd(111) [i.e., strong dependence of S_0 on methane angle of incidence, see Fig. 6(b)]. Therefore on the sides of the particles there will be a lower sticking probability due to the geometry of the system. This means that the Pd particles are expected to have lower sticking probability than the continuous Pd surface, unless they have much higher intrinsic reactivity.

In order to correctly compare the methane sticking probability on the nanoparticles to the Pd(111) surface, we assume the particle shape is a truncated half octahedron with an aspect ratio of 0.4 (i.e., the expected equilibrium shape [2]) and use the measured dependence of sticking probability on normal beam energy for Pd(111) to model what the apparent sticking probability would be on a particle. The sides of the particle account for 88% its surface area. The methane beam is incident on the sides of the particle at 55° from the local surface normal and so the local beam flux will be lower by a factor of $\cos 55^\circ$ compared to the top of the particle. This beam flux difference is accounted for by calculating the fraction of the particle surface area projected into the MgO(100) plane which corresponds to the sides of the particle, 0.81. Thus 81% of the methane beam which strikes Pd will impinge on the sides of the particle and the remainder will impinge at

normal incidence (0°) on the top of the particle. The top of the particle is terminated by the (100) plane of Pd, but sticking data on that surface are not available in the literature. However, by using the normal energy scaling of the sticking probability measured on Pd(111), Eq. (5), we can calculate the expected sticking probability of a methane beam of total energy E on a particle with the same intrinsic reactivity as Pd(111) by

$$S_{\text{expected}}(E) = 0.19 \times 10^{-5.97} 10^{0.0619E} + 0.81 \times 10^{-5.97} 10^{0.0619E \cos^2 55^\circ}, \quad (8)$$

where E is in kJ/mol. We do this for many beam energies in the range shown in Fig. 7 and plot these values as a dash-dot line. The sticking probability measured on the Pd particles is about twice the expected sticking predicted by this model. If this is the actual particle geometry, these data indicate that the Pd nanoparticle surface's intrinsic reactivity for methane dissociation is about twice that for the Pd(111) surface. Note that the second term of Eq. (8) is nearly two orders of magnitude smaller than the first term, due to the strong dependence of sticking probability on incident angle [see Fig. 6(b)]. Thus, in this particle model the apparent sticking is almost completely due to the top facet of the particles with only a negligible contribution from the sides.

Fig. 8 plots the initial sticking probability at 71 kJ/mol as a function of Pd coverage on MgO(100). The sticking was averaged over several experiments at various methane exposures, all in the range of small methane exposure (initial sticking). These average values of sticking probability are plotted vs. Pd coverage (circles). The error bars correspond to one standard deviation of this calculation, based on the scatter in the oxygen saturation coverage, O_{ads} titration, and C_{ads} titration experiments. For the 0.15 and 0.75 ML Pd particles, three experiments are averaged here and eight experiments are averaged for the 1.4 ML Pd particles. The triangular point represents the apparent sticking probability we would expect if the sticking probabilities on the particle surfaces were the same as those measured on Pd(111). This value was obtained directly from properly averaging our measurements on Pd(111), rather than using Eq. (8).

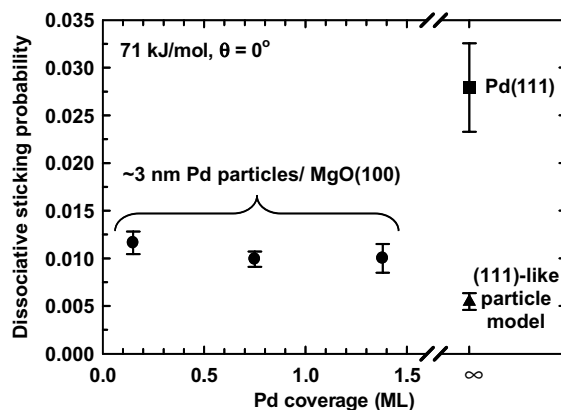


Fig. 8. Methane sticking probability vs. Pd coverage. Circles represent average of several sticking measurements made on Pd nanoparticles at $T_S = 500$ K. The error bars correspond to one standard deviation of the calculated sticking result. The square point is the measured methane sticking probability on Pd(111) at $T_S = 550$ K. The triangular point is a calculation of expected sticking on truncated half octahedron (equilibrium) particle shape based on measurement of S_0 at $\theta = 0^\circ$ and 56° on Pd(111), as described in the text.

We made measurements with a beam energy of 71 kJ/mol at 0° and 56° on Pd(111) and found sticking probabilities of 0.0279 and 0.000183, respectively. The former number we take to be the sticking probability for the tops of the particles and the latter for the sides (angle of incidence of beam on particles sides is $\sim 55^\circ$). Using the correct area fractions for the top and side facets (0.19 and 0.81, resp.) we thus estimate a sticking probability of 0.00545 on the particles, if they have the same intrinsic reactivity as Pd(111). [Note that this is slightly higher than what is predicted by Eq. (8), 0.00508.] It is clear that the average sticking probability on the nanoparticles is about twice that of the Pd(111) surface (filled triangle), assuming the truncated half octahedron geometry. The sticking probability on the Pd(111) surface is represented by the square symbol.

The absolute sticking probability on Pd nanoparticles at 71 kJ/mol is 0.0103 (average of all particle sizes), whereas for a particle with the equilibrium shape but the same reactivity as Pd(111), we predict a sticking probability of 0.00545. (The sticking probability on Pd(111) at normal incidence and this same energy is 0.0279.) The intrinsic sticking probability on the Pd

nanoparticle surface appears to be about twice that on the Pd(111) surface according to this analysis. As noted above, the sides of the particles contribute a negligible amount to the overall methane sticking on the particles and so the observed sticking must be due to sticking on the tops of the particles. The factor of two enhancement observed may be partially due to the particles being terminated by the more open Pd(100) surface rather than the close-packed (111) surface (i.e. sticking may be higher on the more open, lower coordination number particle facets). To our knowledge there has not been a prior study of methane dissociation on Pd(100), but this is consistent with prior studies on Ni(100) and Ni(111), where the dissociative sticking probability of methane is found to be ~ 10 -fold higher on the (100) surface [Ni(111) has S_0 one order of magnitude lower than our results on Pd(111) (0.0015 at 71 kJ/mol) at the conditions of Figs. 4, 5] [28,66]. In the absence of an accurate comparison of methane dissociation on Pd(100) and Pd(111) it is impossible to determine whether the particle sticking is only due to the differences in the packing on these planes.

It was expected at the outset of our study that a more dramatic (i.e., order of magnitude) effect would be observed due to the high density of low coordination atoms on the small nanoparticles. Indeed, on particles in this size range, approximately half of the atoms in the top (100) plane of the cluster are along the edges or at the corners of the top facet. Those edge and corner atoms will have a much lower coordination (6 or less) to other Pd atoms compared to the 8-fold coordination of atoms in the (100) plane. Previous studies have postulated that a low coordination to neighboring metal atoms can allow higher reactivity [1,67]. We find in this case however that even if we assume that the atoms in the (100) plane have the same reactivity as (111) atoms, that these edge atoms would only have at most three-fold higher reactivity due to their low coordination.

4. Conclusions

We have presented measurements of the initial dissociative sticking probability of methane on

the Pd(111) surface as well as on MgO-supported Pd nanoparticles. We have shown that on the Pd(111) surface, the sticking probability follows a “normal energy scaling” and that sticking at high angles of incidence (low normal energy) deviates from this scaling law, possibly due to sticking at defect sites. The strong dependence of sticking probability on normal energy means that sticking measurements by molecular beam on Pd particles will be at a disadvantage to the flat Pd surface due to the fraction of particle surface area at large angles of incidence to the molecular beam. Indeed, we have shown that the sticking probability on the particles appears to be a factor of ~ 3 lower than on the Pd(111) surface. However, we have also shown that by carefully considering the expected equilibrium particle shape and obtaining the area fraction of the particles experimentally, we can make a quantitative comparison between sticking on the particles and sticking on the (111) surface. In this way, we find that the intrinsic reactivity the surfaces of small Pd particles (~ 3 nm) for methane dissociation does not have a significant (e.g., orders of magnitude) enhancement compared to Pd(111), but is at most two times larger. We emphasize the importance of having a good knowledge of particle structure before attempting such a molecular beam study of nanoparticle reactivity. This and the analysis discussed in this paper are of general applicability to future studies of a similar nature. We also observed that O_2 can produce O_{ads} on the Pd particles via a transiently adsorbed, mobile O_2 precursor state on the bare areas of the MgO(100) support. Finally, the saturation density of O_{ads} on the Pd particles is 41% larger than on a continuous Pd film, leading to an interesting induction period in the kinetics of its titration reaction with CO.

Acknowledgements

The authors thank Ian Harrison and Heather Abbott for valuable discussions. BDK and ZD funded by the US Department of Energy Office of Basic Energy Sciences (DOE OBES) Chemical Sciences and Materials Sciences Divisions. CTC acknowledges support by the DOE OBES

Chemical Sciences Division. SLT supported by a graduate student fellowship award from the University of Washington/Pacific Northwest National Laboratory (PNNL) Joint Institute for Nanoscience. All of the experimental work was performed in the Environmental Molecular Sciences Laboratory, a national scientific user facility sponsored by the Department of Energy's Office of Biological and Environmental Research and located at PNNL. PNNL is a multiprogram National Laboratory operated for the US Department of Energy by Battelle Memorial Institute under contract DE-AC06-76RLO 1830.

References

- [1] C.T. Campbell, *Curr. Opin. Solid State Mater.* 3 (1998) 439.
- [2] C.R. Henry, C. Chapon, S. Giorgio, C. Goyhenex, in: R.M. Lambert, G. Pacchioni (Eds.), *Chemisorption and Reactivity on Supported Clusters and Thin Films*, Kluwer Academic Publishers, 1997, p. 117.
- [3] C.R. Henry, *Surf. Sci. Rep.* 31 (1998) 231.
- [4] M. Valden, X. Lai, D.W. Goodman, *Science* 281 (1998) 1647.
- [5] D. Ciuparu, M.R. Lyubovskiy, E. Altman, L.D. Pfefferle, A. Datye, *Catal. Rev. Sci. Eng.* 44 (2002) 593.
- [6] K. Fujimoto, F.H. Ribeiro, M. Avalos-Borja, E. Iglesia, *J. Catal.* 179 (1998) 431.
- [7] J. Wei, E. Iglesia, *J. Phys. Chem. B* 108 (2004) 4094.
- [8] J. Wei, E. Iglesia, *J. Catal.* 225 (2004) 116.
- [9] J. Wei, E. Iglesia, *J. Phys. Chem. B* 108 (2004) 7253.
- [10] C. Becker, C.R. Henry, *Surf. Sci.* 352 (1996) 457.
- [11] C. Duriez, C.R. Henry, C. Chapon, *Surf. Sci.* 253 (1991) 190.
- [12] C.R. Henry, C. Chapon, C. Duriez, *J. Chem. Phys.* 95 (1991) 700.
- [13] C.R. Henry, C. Chapon, C. Goyhenex, R. Monot, *Surf. Sci.* 272 (1992) 283.
- [14] S. Shaikhutdinov, M. Heemeijer, J. Hoffmann, I. Meusel, B. Richter, M. Baumer, H. Kuhlenbeck, J. Libuda, H.J. Freund, R. Oldman, S.D. Jackson, C. Konvicka, M. Schmid, P. Varga, *Surf. Sci.* 501 (2002) 283.
- [15] E.S. Putna, J.M. Vohs, R.J. Gorte, *Surf. Sci.* 391 (1997) L1178.
- [16] M.C. McMaster, R.J. Madix, *J. Chem. Phys.* 98 (1993) 9963.
- [17] A.V. Hamza, H.-P. Steinruck, R.J. Madix, *J. Chem. Phys.* 86 (1987) 6506.
- [18] C.B. Mullins, W.H. Weinberg, *J. Vac. Sci. Technol. A* 8 (1990) 2458.
- [19] C.R. Arumainayagam, M.C. McMaster, G.R. Schoofs, R.J. Madix, *Surf. Sci.* 222 (1989) 213.
- [20] V.A. Ukraintsev, I. Harrison, *J. Chem. Phys.* 101 (1994) 1564.
- [21] V.A. Ukraintsev, I. Harrison, *Surf. Sci.* 286 (1993) L571.
- [22] M. Hirsimaki, S. Paavilainen, J.A. Nieminen, M. Valden, *Surf. Sci.* 482 (2001) 171.
- [23] A.C. Luntz, D.S. Bethune, *J. Chem. Phys.* 90 (1989) 1274.
- [24] A. Bukoski, D. Blumling, I. Harrison, *J. Chem. Phys.* 118 (2003) 843.
- [25] J. Harris, J. Simon, A.C. Luntz, C.B. Mullins, C.T. Rettner, *Phys. Rev. Lett.* 67 (1991) 652.
- [26] G.R. Schoofs, C.R. Arumainayagam, M.C. McMaster, R.J. Madix, *Surf. Sci.* 215 (1989) 1.
- [27] M. Valden, J. Pere, M. Hirsimaki, S. Suhonen, M. Pessa, *Surf. Sci.* 377 (1997) 605.
- [28] M.B. Lee, Q.Y. Yang, S.L. Tang, S.T. Ceyer, *J. Chem. Phys.* 85 (1986) 1693.
- [29] H.L. Abbott, A. Bukoski, D.F. Kavulak, I. Harrison, *J. Chem. Phys.* 119 (2003) 6407.
- [30] D.C. Seets, C.T. Reeves, B.A. Ferguson, M.C. Wheeler, C.B. Mullins, *J. Chem. Phys.* 107 (1997) 10229.
- [31] H.L. Abbott, I. Harrison, *J. Phys. Chem. B* 109 (2005) 10371.
- [32] C.T. Rettner, H.E. Pfnur, D.J. Auerbach, *Phys. Rev. Lett.* 54 (1985) 2716.
- [33] A.V. Walker, D.A. King, *J. Chem. Phys.* 112 (2000) 4739.
- [34] C.B. Mullins, W.H. Weinberg, *J. Chem. Phys.* 92 (1990) 4508.
- [35] Z. Dohnalek, G.A. Kimmel, S.A. Joyce, P. Ayotte, R.S. Smith, B.D. Kay, *J. Phys. Chem. B* 105 (2001) 3747.
- [36] M.C. Wu, J.S. Corneille, J.W. He, C.A. Estrada, D.W. Goodman, *J. Vac. Sci. Technol. A* 10 (1992) 1467.
- [37] M.C. Wu, J.S. Corneille, C.A. Estrada, J.W. He, D.W. Goodman, *Chem. Phys. Lett.* 182 (1991) 472.
- [38] S.L. Tait, Z. Dohnalek, C.T. Campbell, B.D. Kay, *J. Chem. Phys.* 122 (2005) 164707.
- [39] S.L. Tait, Z. Dohnalek, C.T. Campbell, B.D. Kay, *J. Chem. Phys.* 122 (2005) 164708.
- [40] C.R. Henry, C. Chapon, C. Duriez, S. Giorgio, *Surf. Sci.* 253 (1991) 177.
- [41] G. Haas, A. Menck, H. Brune, J.V. Barth, J.A. Venables, K. Kern, *Phys. Rev. B* 61 (2000) 11105.
- [42] Z. Dohnalek, J. Kim, B.D. Kay, unpublished.
- [43] X. Guo, J.T. Yates Jr., *J. Chem. Phys.* 90 (1989) 11105.
- [44] B. Klotzer, W. Unterberger, K. Hayek, *Surf. Sci.* 532–535 (2003) 142.
- [45] J.Z. Larese, *Physica B* 248 (1998) 297.
- [46] J.P. Coulomb, K. Madih, B. Croset, H.J. Lauter, *Phys. Rev. Lett.* 54 (1985) 1536.
- [47] R.C. Weast (Ed.), *CRC Handbook of Chemistry and Physics*, 53rd ed., CRC Press, Inc., Boca Raton, Florida, 1972.
- [48] D.R. Miller, in: G. Scoles (Ed.), *Atomic and Molecular Beam Methods*, 1, Oxford University Press, Oxford, 1988.

- [49] J.B. Anderson, in: P.P. Wegener (Ed.), *Molecular Beams and Low Density Gas Dynamics*, Dekker, New York, 1974.
- [50] S.L. Tait, L.T. Ngo, Q. Yu, S.C. Fain, C.T. Campbell, *J. Chem. Phys.* 122 (2005) 064712.
- [51] G.E. Gdowski, T.E. Felter, *J. Vac. Sci. Technol. A* 4 (1986) 1409.
- [52] A.C. Luntz, J. Harris, *Surf. Sci.* 258 (1991) 397.
- [53] S.W. Pauls, C.T. Campbell, *Surf. Sci.* 226 (1990) 250.
- [54] T. Engel, *J. Chem. Phys.* 69 (1978) 373.
- [55] G. Zheng, E.I. Altman, *Surf. Sci.* 462 (2000) 151.
- [56] D.A. King, M.G. Wells, *Surf. Sci.* 29 (1972) 454.
- [57] U. Diebold, J.-M. Pan, T.E. Madey, *Phys. Rev. B* 47 (1993) 3868.
- [58] S. Tanuma, C.J. Powell, D.R. Penn, *Surf. Interface Anal.* 17 (1991) 911.
- [59] R. Kern, in: I. Sunagawa (Ed.), *Morphology of Crystals*, A, Terra Scientific Publishing Company, Tokyo, 1987, p. 77.
- [60] C.R. Henry, M. Meunier, *Mater. Sci. Eng. A* 217/218 (1996) 239.
- [61] T. Engel, G. Ertl, *J. Chem. Phys.* 69 (1978) 1267.
- [62] C.L. Kao, R.J. Madix, *J. Phys. Chem. B* 106 (2002) 8248.
- [63] A. Imre, D.L. Beke, E. Gontier-Moya, I.A. Szabo, E. Gillet, *Appl. Phys. A* 71 (2000) 19.
- [64] G.A. Kimmel, M. Persson, Z. Dohnalek, B.D. Kay, *J. Chem. Phys.* 119 (2003) 6776.
- [65] M. Hirsimaki, M. Valden, *Surf. Sci.* 562 (2004) 284.
- [66] P.M. Holmblad, J. Wambach, I. Chorkendorff, *J. Chem. Phys.* 102 (1995) 8255.
- [67] A.S. McLeod, L.F. Gladden, *J. Catal.* 173 (1998) 43.